University of Bath

Alternative formats

If you require this document in an alternative format, please contact:
openaccess@bath.ac.uk

Extended Minimum Copper Loss Range Fault-Tolerant Control for Dual Three-Phase PMSM

Haolin Zheng[1], Xiaoze Pei[1], Constantinos Liagas[2], Chris Brace[1], Xianwu Zeng[1]

1. Institute of Advance Automotive Propulsion System, University of Bath

2. EPSRC Centre for Doctoral Training in Advanced Automotive Propulsion Systems, University of Bath

Abstract-This paper studies the single open-circuit failure (OCF) in dual three-phase permanent magnet synchronous motors (DT-PMSM) in transport electrification where wide speed range and torque operation range (TOR) are required. A new control scheme is proposed to extend the TOR with minimum copper loss based on the well-established fault-tolerant control strategy minimum loss (ML) and maximum torque (MT). The ML strategy allows the demanded torque at the reference speed to be delivered with minimum copper loss. The MT strategy presents wider torque capability in post-fault operation without exceeding the current limit, whilst copper loss within the stator winding is not optimized. However, there is a gap in the permissible TOR of these two strategies. A simple switch of strategy, from ML to MT when the limit of ML's TOR is reached, would result in excessive copper loss. The proposed full-torque-operation-range minimum loss (FTOR-ML) in this paper is proposed to mitigate the excessive copper loss. The novel FTOR-ML for the DT-PMSM under OCF for different winding configurations, single (1N) and isolated neutral point (2N), combines the merit of ML and MT where the entire TOR of MT is achieved with minimum copper loss. The analytical solution of FTOR-ML is derived in this paper for both winding configurations. Experimental result demonstrates the combined merit and effectiveness of the proposed control scheme.

Index – Fault-Tolerant Control, Dual Three-Phase Permanent Magnet Synchronous Motor (DT-PMSM), Open-Circuit Fault, Minimum Copper Loss

I. INTRODUCTION

Dual three-phase permanent magnet synchronous motor (DT-PMSM) has attracted increasing attention in the transportation industry for its high-power density and fault-tolerant capability [1-4]. Fig. 1 outlines the electromagnetic configuration of a typical dual 3-phase PMSM where the second set of 3-phase winding "uvw" lags the first set "abc" by 30°.
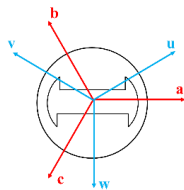

Fig. 1 Winding arrangement of DT- PMSM

There are multiple types of faults that may occur during operation in an electrical machine, including short circuit and open circuit in phase, inverter, switch and interturn [5]. This paper focuses on the single open-circuit fault (OCF) where phase *w* is open circuit, i.e. $i_w = 0$.

In order to achieve smooth and ripple-free post-fault operation, the primary objective of fault-tolerant control (FTC) is to control the motor so that a stable rotating magnetomotive force is maintained. There are two well-established strategies in obtaining post-fault current reference.

- Minimum loss (ML) [6-8]– The goal is to minimize the copper loss. This strategy usually results in phase currents of different rms value.

- Maximum torque (MT) [9-12]– In this strategy, the phase currents are forced to have the same rms value, i.e. the same waveform with different phase angle, to fully utilise the current capability so that torque output can be maximised. There is an exception in the case of isolated neutral points, where not all healthy phases are utilised, which will be demonstrated in section III.

Apart of these two strategies, state-of-the-art FTC for DT-PMSM includes the use of a hybrid neutral point that exploits the field-weakening operation at high motor speed [13]. It combines the merits of different neutral point connection with connected neutral point (1N) and isolated neutral points (2N) that extends the torque and speed range. The stator winding with 1N has higher torque range due to better current usage and 2N offers wider speed range due to more-efficient voltage usage. Hybrid MLMT control is proposed in [6, 14, 15] for 2N. Che, H.S. *et al* has applied emulation to find the optimum combination of the design variable K across all permissible *K*, which includes both strategies [6]. In [14], the authors have further unified the single 3-phase mode, that only utilises the healthy winding set for post-fault operation, together with ML and MT. Geng *et al* [15] proposed a FTC scheme, the natural full range minimum loss (FRML), where seamless transition from ML to MT can be achieved without the need of fault detection scheme, and hence a simpler overall control scheme for OCF. These three papers [6, 14, 15] all combine the merits of ML and MT allowing the motor to operate with minimum copper loss under single OCF, for permissible reference torque, while the current limit is not exceeded, but the 1N condition has not yet been investigated and discussed. To this end, a more recent paper, [16], has considered the case of 1N, which proposed a MT-based optimisation algorithm to achieve minimum torque ripple considering the non-sinusoidal back EMF. However, the optimized solution from [16] only addresses scenarios where currents in all phases are saturated, leaving significant room for optimization when currents are below their limits. Furthermore, in [17], the author has proposed an online current optimisation algorithm for a symmetrical multi-phase machine under OCF across the entire TOR so that preserving the controller memory in pre-stored look-up tables for any offline optimisation algorithm is no longer required. However, multi-phase machine with asymmetrical windings is not considered and the online optimisation algorithm still requires considerable computational resources.

This paper is an extended work of [18], which presents an FTC scheme that is applicable for the entire TOR in an asymmetrical DT-PMSM to achieve minimum copper loss, for both 1N and 2N. The novelty is that the analytical solution for the design variable K is derived so that neither pre-stored look-up tables nor online optimisation are required. The solution is obtained by analytically solving the optimisation problem, using the Lagrange multiplier method. The outcome not only guarantees minimum copper loss across the entire TOR, but also paves the way to exploit a wider speed range under OCF for the

calculation of the reference current where the DC bus voltage limit becomes a constraint. The solution for 1N is numerically calculated. The result derived is universal regardless of motor parameters.

This paper is organized as followed. The mathematical model of a DT-PMSM under OCF in phase w is derived in section II using the vector space decomposition (VSD), for both 1N and 2N. In section III, the two FTC strategies ML and MT and their associated TOR are first studied and derived, followed by which, the full-torque-operation-range minimum loss (FTOR-ML) strategy is proposed. In section IV, experimental work is carried out, to validate the proposed control scheme and results are discussed. Finally, conclusion is drawn and future work is inspired based on the analysis and discussion of the experimental outcome.

II. CONTROL AND MODELLING OF FAULTY DT-PMSM

Similar to the conventional 3-phase machine, the 6-phase electrical quantities $f_{abc,uvw}$, where $f \in \{ U,I,\psi \}$, are mapped to the stationary frame using the amplitude invariant Clarke Transform matrix for VSD, $f_{\alpha\beta,XY,o_1 o_2} = T_C f_{abc,uvw}$ [19].

$$T_C = \frac{1}{3}\begin{bmatrix} 1 & -\frac{1}{2} & -\frac{1}{2} & \frac{\sqrt{3}}{2} & -\frac{\sqrt{3}}{2} & 0 \\ 0 & \frac{\sqrt{3}}{2} & -\frac{\sqrt{3}}{2} & \frac{1}{2} & \frac{1}{2} & -1 \\ 1 & -\frac{1}{2} & -\frac{1}{2} & -\frac{\sqrt{3}}{2} & \frac{\sqrt{3}}{2} & 0 \\ 0 & -\frac{\sqrt{3}}{2} & \frac{\sqrt{3}}{2} & \frac{1}{2} & \frac{1}{2} & -1 \\ 1 & 1 & 1 & 0 & 0 & 0 \\ 0 & 0 & 0 & 1 & 1 & 1 \end{bmatrix}. \quad (1)$$

The first two rows define the electromagnetic-torque-relevant αβ subspace. The quantities in this dual 3-phase αβ subspace can be considered as the sum of the quantities from each set of the 3-phase winding that is projected to the stationary frame. The third and fourth row defines the non-electromagnetic-torque-relevant XY subspace, and it can be regarded as the differences between the 2 sets of winding. It reflects the imbalance level between the 2 sets. The last two rows are related to the zero-sequence quantities, which is more of interest in the case of 1N and can be ignored in the 2N case because of Kirchhoff's Current Law. Under the healthy condition, the quantities on the XY and zero-sequence subspace should be controlled to zero, to avoid imbalance within and between the winding sets and thus any excessive copper loss.

In order to maintain stable and ripple-free torque output, the reference currents in the stationary αβ subspace must be a pair of orthogonal AC phasors with identical magnitude such that the currents in the synchronous DQ subspace are a DC value. Hence, for any random AC phasors in the non-torque-generation XY subspace, they can be expressed as

$$\begin{cases} i_X = K_X^\alpha i_\alpha + K_X^\beta i_\beta \\ i_Y = K_Y^\alpha i_\alpha + K_Y^\beta i_\beta \end{cases}, \quad (2)$$

where K_n^m ($n = X,Y$; $m = \alpha, \beta$) are the design variables for the optimisation algorithm in next section. The objective of ML/MT and the proposed FTOR-ML can be achieved by searching for optimum design variables.

In the case of 2N connection, according to the Kirchhoff's Current Law, $i_u + i_v = 0$. By substituting this into the DT Clarke Transform, the following identities are derived,

$$\begin{cases} i_Y = -i_\beta = \frac{1}{3} \times \left(-\frac{\sqrt{3}}{2} i_b + \frac{\sqrt{3}}{2} i_c \right) \\ i_{o_1} = i_{o_2} = 0 \end{cases} \quad (3)$$

Hence, there are 3 degrees of freedom for the FTC of DT-PMSM in single OCF with 2N, i.e. i_α i_β and i_X. With equations (2) and (3), the following equation is derived as,

$$i_{\alpha\beta,XY,o_1 o_2} = T_{2N} \cdot i_{\alpha\beta} \quad (4)$$

where $i_{\alpha\beta} = [i_\alpha \ i_\beta]^T$; $T_{2N} = \begin{bmatrix} 1 & 0 & K_X^\alpha & 0 & 0 & 0 \\ 0 & 1 & K_X^\beta & -1 & 0 & 0 \end{bmatrix}^T$.

On the other hand, in the case of a connected neutral point (1N), $i_a + i_b + i_c + i_u + i_v = 0$. Substituting this into the Clarke Transform, (5) is obtained as

$$\begin{cases} i_{o_1} = -i_{o_2} \\ i_{o_2} = i_\beta + i_Y \end{cases}. \quad (5)$$

Therefore, there are 4 degrees of freedom with 1N to be controlled - i_α, i_β, i_X and i_Y. (4) with 2N connection becomes,

$$i_{\alpha\beta,XY,o_1 o_2} = T_{1N} \cdot i_{\alpha\beta} \quad (6)$$

where $T_{1N} = \begin{bmatrix} 1 & 0 & K_X^\alpha & K_Y^\alpha & -K_Y^\alpha & K_Y^\alpha \\ 0 & 1 & K_X^\beta & K_Y^\beta & -1-K_Y^\beta & 1+K_Y^\beta \end{bmatrix}^T$.

Furthermore, by using the Park transform matrix for the 6-phase winding, the quantities in the stationary frame are transferred to the synchronous DQ subspace, DQz harmonics subspace and the $O_1 O_2$ zero-sequence subspace $f_{dq,dqz,o_1 o_2} = T_{P6} f_{\alpha\beta,XY,o_1 o_2}$, and

$$T_{P6} = \begin{bmatrix} T_P(\theta_e) & O_2 & O_2 \\ O_2 & T_P(-\theta_e) & O_2 \\ O_2 & O_2 & I_2 \end{bmatrix} \quad (7)$$

where O_2 and I_2 are the 2×2 zeros and identity matrix; θ_e is the electrical angle and

$$T_P(\theta_e) = \begin{bmatrix} \cos(\theta_e) & \sin(\theta_e) \\ -\sin(\theta_e) & \cos(\theta_e) \end{bmatrix}. \quad (8)$$

After the transformation, the mathematical model of the DT-PMSM in the synchronous frame is defined as,

$$\begin{cases} u_d = 1^{st} Row(R_s)i_{dq,dqz,o_1 o_2} - \omega_e L_q i_q + L_d \frac{di_d}{dt} \\ u_q = 2^{nd} Row(R_s)i_{dq,dqz,o_1 o_2} + \omega_e L_d i_d + \omega_e \psi_f + L_q \frac{di_q}{dt} \\ u_{dz} = 3^{rd} Row(R_s)i_{dq,dqz,o_1 o_2} - \omega_e L_{qz} i_{qz} + L_{dz} \frac{di_{dz}}{dt} \\ u_{qz} = 4^{th} Row(R_s)i_{dq,dqz,o_1 o_2} + \omega_e L_{dz} i_{dz} + L_{qz} \frac{di_{qz}}{dt} \end{cases} \quad (9)$$

$$\begin{cases} u_{o_1} = 5^{th} Row(R_s)i_{dq,dqz,o_1 o_2} - \omega_e L_{o_2} i_{o_2} + L_{o_1} \frac{di_{o_1}}{dt} \\ u_{o_2} = 6^{th} Row(R_s)i_{dq,dqz,o_1 o_2} + \omega_e L_{o_1} i_{o_1} + L_{o_2} \frac{di_{o_2}}{dt} \end{cases} \quad (10)$$

where ω_e is the electrical frequency; ψ_f is the flux linkage induced by the permanent magnet; L_j ($j = d, q, dz, qz, o_1, o_2$) is the decoupled inductance on their corresponding axis respectively, $L_{dq,dqz,o1o2} = T_c T_{p6} \times L_{abc,uvw} \times (T_c T_{p6})^{-1}$, and

$$L_{abc,uvw} = \begin{bmatrix} L_{aa} & M_{ab} & M_{ac} & M_{au} & M_{av} & M_{aw} \\ M_{ba} & L_{bb} & M_{bc} & M_{bu} & M_{bv} & M_{bw} \\ M_{ca} & M_{cb} & L_{cc} & M_{cu} & M_{cv} & M_{cw} \\ M_{ua} & M_{ub} & M_{uc} & L_{uu} & M_{uv} & M_{uw} \\ M_{va} & M_{vb} & M_{vc} & M_{vu} & L_{vv} & M_{vw} \\ M_{wa} & M_{wb} & M_{wc} & M_{wu} & M_{wv} & L_{ww} \end{bmatrix}; \quad (11)$$

R_s is the resistance matrix in the synchronous frames, $R_s = T_c T_{p6} \times R_{abc,uvw} \times (T_c T_{p6})^{-1}$, and $R_{abc,uvw} = diags(R_a, R_b, R_c, R_u, R_v, R_w)$. It should be noted that during simulation, resistance in the faulty phase w should be set to a sufficiently large value to mimic the open-circuit situation. This imbalanced stator resistance leads to a fluctuating, coupled resistive voltage drop in the synchronous frames. This is different from the healthy

condition where resistive voltage drop is a pure DC value depending solely on the decoupled currents in each axis.

It is worth noting that the optimisation algorithm proposed in next section is valid regardless of motor parameters and hence nonlinearities such as cross-coupling and magnetic saturation does not need to be considered. Therefore, the electrical mathematical models in (9) and (10) are linearly modelled for simplicity except for the resistive voltage drop.

Fig. 2 outlines the complete control scheme of the fault-tolerant control for DT-PMSM. The scheme is almost identical to a conventional field-oriented control scheme using VSD in the case of 2N, with a 3rd proportional-resonant controller being applied to regulate the 3rd order harmonics projected on the zero-sequence subspace in 1N. In order to guarantee minimum modification, while the control scheme in healthy condition is preserved, second and first order resonant controllers are added to the synchronous DQ/DQz-frame and zero-sequence subspace respectively to regulate the reference current with 2nd and 1st-order component, as demonstrated in (17), where $i_s^* = \sqrt{i_d^{*2} + i_q^{*2}}$ and $tan(\phi_{dqz}) =$

$$\left[\left(K_X^\beta - K_Y^\alpha \right) i_d^* - \left(K_X^\alpha + K_Y^\beta \right) i_q^* \right] \Big/ \left(K_X^\alpha + K_Y^\beta \right) i_d^* + \left(K_X^\beta - K_Y^\alpha \right) i_q^*.$$

III. OPTIMISATION ALGORITHM OF POST-FAULT OPERATION

A. Minimum Loss and Maximum Torque

As long as the current in the electromagnetic-torque-relevant $\alpha\beta$ subspace is maintained, a stable torque and hence smooth operation can be guaranteed. Therefore, i_α and i_β are solely dependent on the reference torque at specific operating conditions, and hence they can be regarded as a constant value that is not manipulatable during the optimisation.

1. Isolated Neutral Point (2N)

To achieve minimum copper loss with 2N, the objective can be mathematically expressed as

$$\min_{K_X^\alpha, K_X^\beta \in R} i_X^2 + i_Y^2 + i_{o_1}^2 + i_{o_2}^2. \tag{12}$$

With (2), (3) and the matrix T_{2N}, (12) is equivalent to

$$\min_{K_X^\alpha, K_X^\beta \in R} F\left(K_X^\alpha, K_X^\beta \right). \tag{13}$$

where $F\left(K_X^\alpha, K_X^\beta \right) = K_X^{\alpha 2} + K_X^{\beta 2} + 1$. The solution of this optimisation problem is apparent and minimum loss is achieved when,

$$K_X^\alpha = K_X^\beta = 0. \tag{14}$$

The corresponding phase current waveform is calculated as $i_{abc,uvw} = M_{2N} \cdot i_{\alpha\beta}$, where

$$M_{2N} = T_C^{-1} \cdot T_{2N} = \begin{bmatrix} 1 + K_X^\alpha & -K_X^\beta \\ -\frac{1}{2} - \frac{1}{2} K_X^\alpha & \sqrt{3} + \frac{1}{2} K_X^\beta \\ -\frac{1}{2} - \frac{1}{2} K_X^\alpha & -\sqrt{3} + \frac{1}{2} K_X^\beta \\ \frac{\sqrt{3}}{2} - \frac{\sqrt{3}}{2} K_X^\alpha & \frac{\sqrt{3}}{2} K_X^\beta \\ -\frac{\sqrt{3}}{2} + \frac{\sqrt{3}}{2} K_X^\alpha & -\frac{\sqrt{3}}{2} K_X^\beta \\ 0 & 0 \end{bmatrix}, \tag{15}$$

and hence

$$\begin{cases} i_a = I_s \cos(\omega_e t + \theta_T) \\ i_b = \frac{\sqrt{13}}{2} \times I_s \cos(\omega_e t - 106.1° + \theta_T) \\ i_c = \frac{\sqrt{13}}{2} \times I_s \cos(\omega_e t + 106.1° + \theta_T) \\ i_u = \frac{\sqrt{3}}{2} \times I_s \cos(\omega_e t + \theta_T) \\ i_v = \frac{\sqrt{3}}{2} \times I_s \cos(\omega_e t - \pi + \theta_T) \end{cases} \tag{16}$$

where I_s is the magnitude of the current vector; θ_T is the torque

$$\left[i_{dz}^* \ i_{qz}^* \ i_{o_1}^* \ i_{o_2}^* \right]^T = \begin{bmatrix} T_P(-\theta_e) & O_2 \\ O_2 & I_2 \end{bmatrix} i_{XY,o_1 o_2} = \begin{bmatrix} T_P(-\theta_e) & O_2 \\ O_2 & I_2 \end{bmatrix} \cdot \begin{bmatrix} K_X^\alpha & K_Y^\alpha & -K_Y^\alpha & K_Y^\alpha \\ K_X^\beta & K_Y^\beta & -1 - K_Y^\beta & 1 + K_Y^\beta \end{bmatrix}^T \cdot i_{\alpha\beta}$$

$$= \begin{bmatrix} T_P(-\theta_e) & O_2 \\ O_2 & I_2 \end{bmatrix} \cdot \begin{bmatrix} K_X^\alpha & K_Y^\alpha & -K_Y^\alpha & K_Y^\alpha \\ K_X^\beta & K_Y^\beta & -1 - K_Y^\beta & 1 + K_Y^\beta \end{bmatrix}^T \cdot T_P^{-1}(\theta_e) \cdot \left[i_d^* \ i_q^* \right]^T$$

$$= \begin{bmatrix} \frac{1}{2} \left[\left(K_X^\alpha - K_Y^\beta \right) i_d^* + \left(K_X^\beta + K_Y^\alpha \right) i_q^* \right] + \frac{1}{2} i_s^* \sqrt{\left(K_X^\alpha + K_Y^\beta \right)^2 + \left(K_X^\beta - K_Y^\alpha \right)^2} \cos(2\theta_e - \phi_{dqz}) \\ \frac{1}{2} \left[\left(K_X^\beta + K_Y^\alpha \right) i_d^* + \left(K_Y^\beta - K_X^\alpha \right) i_q^* \right] + \frac{1}{2} i_s^* \sqrt{\left(K_X^\alpha + K_Y^\beta \right)^2 + \left(K_X^\beta - K_Y^\alpha \right)^2} \sin(2\theta_e - \phi_{dqz}) \\ -\left[K_Y^\alpha i_d^* + \left(1 + K_Y^\beta \right) i_q^* \right] \cos(\theta_e) - \left[\left(1 + K_Y^\beta \right) i_d^* - K_Y^\alpha i_q^* \right] \sin(\theta_e) \\ \left[K_Y^\alpha i_d^* + \left(1 + K_Y^\beta \right) i_q^* \right] \cos(\theta_e) + \left[\left(1 + K_Y^\beta \right) i_d^* - K_Y^\alpha i_q^* \right] \sin(\theta_e) \end{bmatrix} \tag{17}$$
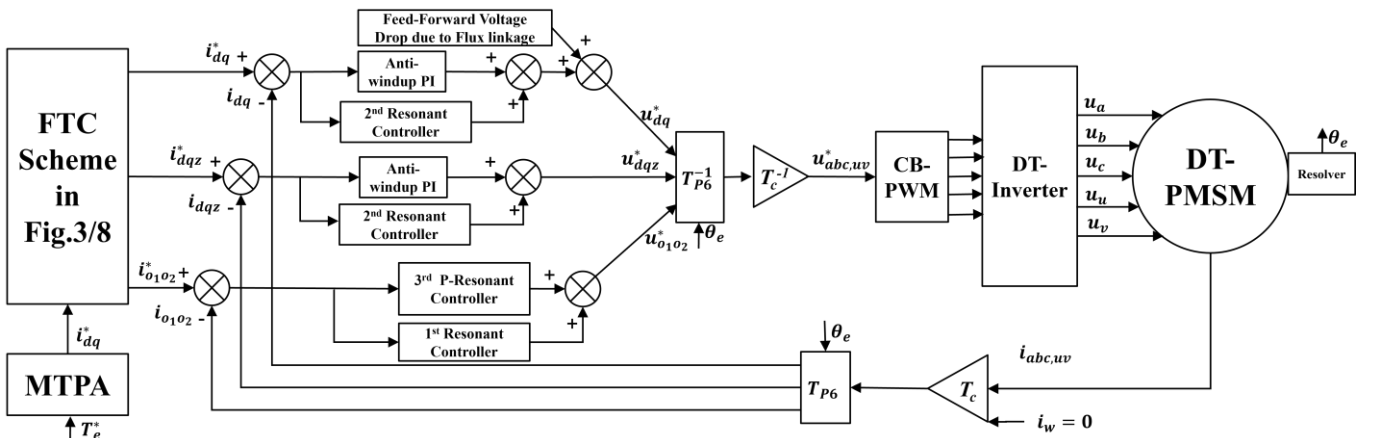

Fig. 2 FTC control scheme for DT-PMSM with single OCF

angle in the synchronous DQ subspace. It is worth noting that I_s is the magnitude of the current phasor i_α and i_β in the amplitude invariant transformation. Thus, the derating factor, which is the extent of reduction of torque output, of the minimum loss control is $\frac{2}{\sqrt{13}} = 55.47\%$.

On the other hand, to maximise torque output while preserving the current limit, the objective is to maximise the derating factor, which is mathematically expressed as

$$\min_{K_X^\alpha, K_X^\beta \in R} [\text{Max}(I_a, I_b, I_c, I_u, I_v)]. \qquad (18)$$

where I_a-I_v are the amplitudes of the corresponding phase currents under single OCF, defined according to (15) as,

$$I_j = \sqrt{2} \times RMS(i^{th}\ row\ of\ M_{2N}) \times i_{pu} \times I_{max} \qquad (19)$$

where $j = a, b, c, u, v$ corresponding to the 1st to 5th row of M_{2N} respectively; i_{pu} is the per-unit value of I_s, $i_{pu} = \frac{I_s}{I_{max}}$, and I_{max} is the current limit.

By applying the optimisation algorithm in MATLAB using the function "fminsearch", the solution always converges to an identical result regardless of the initial value. The optimum design values for MT with 2N are,

$$K_X^\alpha = -1; K_X^\beta = 0. \qquad (20)$$

Their corresponding phase current waveforms are,

$$\begin{cases} i_a = 0 \\ i_b = \sqrt{3}I_s \cos\left(\omega_e t - \frac{\pi}{2} + \theta_T\right) \\ i_c = \sqrt{3}I_s \cos\left(\omega_e t + \frac{\pi}{2} + \theta_T\right) \\ i_u = \sqrt{3}I_s \cos(\omega_e t + \theta_T) \\ i_v = \sqrt{3}I_s \cos(\omega_e t - \pi + \theta_T) \end{cases} \qquad (21)$$

and the derating factor is $\frac{1}{\sqrt{3}} = 57.735\%$.

2. Single Neutral Point(1N)

In the case of 1N, the objective for ML in (12) holds and with the matrix T_{1N} it is equivalent to,

$$\min_{K_X^\alpha, K_X^\beta, K_Y^\alpha, K_Y^\beta \in R} F\left(K_X^\alpha, K_X^\beta, K_Y^\alpha, K_Y^\beta\right). \qquad (22)$$

where $F = K_X^{\alpha 2} + K_X^{\beta 2} + 3K_Y^{\alpha 2} + 3K_Y^{\beta 2} + 4K_Y^\beta + 2$. Its solution is obtained by solving the Jacobian Matrix of F, which gives the result as

$$K_X^\alpha = K_X^\beta = K_Y^\alpha = 0;\ K_Y^\beta = -\frac{2}{3} \qquad (23)$$

The corresponding waveforms of the healthy phase current are derived by $i_{abc,uvw} = M_{1N} \cdot i_{\alpha\beta}$ in (28). The matrix M_{1N} is derived in (29). The derating factor is $\frac{6}{\sqrt{88+20\sqrt{3}}} = 54.18\%$.

For maximum torque control, the objective function in equation (18) holds except that in the case of 1N there are 4 design variables, expressed as,

$$\min_{K_X^\alpha, K_X^\beta, K_Y^\alpha, K_Y^\beta \in R} [\text{Max}(I_a, I_b, I_c, I_u, I_v)] \qquad (24)$$

where

$$I_j = \sqrt{2} \times RMS(i^{th}\ row\ of\ M_{1N}) \times i_{pu} \times I_{max} \qquad (25)$$

It is not feasible to solve this optimisation problem with 4 design variables using "fminsearch" since the result is not able to converge to the same value with different initial value. Instead, "global search" within the optimisation toolbox in MATLAB is used to find the global minimum as it always converges to the same value. The optimum result is

$$\begin{array}{ll} K_X^\alpha = -0.296 & K_X^\beta = -0.754 \\ K_Y^\alpha = -0.209 & K_Y^\beta = -0.641 \end{array} \qquad (26)$$

and the corresponding waveform of phase current is shown below, where the derating factor is equal to $1/1.44 = 69.44\%$.

$$\begin{cases} i_a = 1.44 \times I_s \cos(\omega_e t + 50.6° + \theta_T) \\ i_b = 1.44 \times I_s \cos(\omega_e t - 88.5° + \theta_T) \\ i_c = 1.44 \times I_s \cos(\omega_e t + 103° + \theta_T) \\ i_u = 1.44 \times I_s \cos(\omega_e t - 55.8° + \theta_T) \\ i_v = 1.44 \times I_s \cos(\omega_e t + 175.4° + \theta_T) \end{cases} \qquad (27)$$

To sum up, Table 1 shows the 4 design variables for ML and MT with different configuration of neutral point in single OCF.

Table 1 Optimum Design Variable for FTC under Single OCF

	2N		1N	
	ML	MT	ML	MT
K_X^α	0	-1	0	-0.296
K_X^β	0	0	0	-0.754
K_Y^α	0	0	0	-0.21
K_Y^β	-1	-1	-2/3	-0.641
Derating factor	55.47%	57.74%	54.18%	69.44%

It is clear that in post-fault operation, the ML strategy is applied for minimum copper losses and maintained until the phase current that has highest amplitude among the 5 healthy phases has reached the current limit. This occurs when the magnitude of the current vector I_s reaches 55.47% of the current limit, i.e. electromagnetic torque output reaches the same percentage of the maximum torque output in the healthy condition. To further increase the torque output, the MT strategy can be applied after the current limit for ML is reached. However, there is a gap between the ML and MT, derating factor from 55.47% to 57.74% and if a simple switch of strategy is applied, the performance may not be optimum in terms of losses. In the transition region of torque output from ML to MT, there is always some current usage reserved, which can be utilised to improve copper loss, until the current limit is reached. Moreover, such a gap in the case of 1N connection is even greater, with derating factor increasing from 54.18% with ML to 69.44% with MT.

$$\begin{cases} i_a = \frac{\sqrt{10}}{3}I_s \cos(\omega_e t + 18.43° + \theta_T) \\ i_b = \frac{\sqrt{88 - 20\sqrt{3}}}{6}I_s \cos(\omega_e t - 114.25° + \theta_T) \\ i_c = \frac{\sqrt{88 + 20\sqrt{3}}}{6}I_s \cos(\omega_e t + 105.72° + \theta_T) \\ i_u = I_s \cos\left(\omega_e t - \frac{\pi}{6} + \theta_T\right) \\ i_v = I_s \cos\left(\omega_e t - \frac{5}{6}\pi + \theta_T\right) \end{cases} \qquad (28)$$

$$M_{1N} = T_C^{-1} \cdot T_{1N}$$
$$= \begin{bmatrix} 1 + K_X^\alpha - K_Y^\alpha & -\frac{1}{2} - \frac{1}{2}K_X^\alpha - \left(\frac{\sqrt{3}}{2} + 1\right)K_Y^\alpha & -\frac{1}{2} - \frac{1}{2}K_X^\alpha + \left(\frac{\sqrt{3}}{2} + 1\right)K_Y^\alpha & \cdots \\ -1 + K_X^\beta - K_Y^\beta & \frac{\sqrt{3}}{2} - 1 - \frac{1}{2}K_X^\beta - \left(\frac{\sqrt{3}}{2} + 1\right)K_Y^\beta & -\frac{\sqrt{3}}{2} - 1 - \frac{1}{2}K_X^\beta + \left(\frac{\sqrt{3}}{2} - 1\right)K_Y^\beta & \cdots \\ \cdots & \frac{\sqrt{3}}{2} - \frac{\sqrt{3}}{2}K_X^\alpha + \frac{3}{2}K_Y^\alpha & -\frac{\sqrt{3}}{2} + \frac{\sqrt{3}}{2}K_X^\alpha + \frac{3}{2}K_Y^\alpha & 0 \\ \cdots & \frac{3}{2} - \frac{\sqrt{3}}{2}K_X^\beta + \frac{3}{2}K_Y^\beta & \frac{3}{2} + \frac{\sqrt{3}}{2}K_X^\beta + \frac{3}{2}K_Y^\beta & 0 \end{bmatrix}^T \qquad (29)$$

B. Full-Torque-Operation-Range Minimum Loss

To fill the gap between ML and MT so that the torque operation region is maximised while loss is minimised, the FTOR-ML is proposed to achieve minimum copper loss when delivering torque above the limit of ML. To realise ML, the objective function in (13) and (22) still hold, except that extra constraints need to be applied to comply with the phase current limit.

1. Isolated Neutral Point (2N)

It is obvious that the solution in (14) for ML with 2N is the global minimum without any constraint. To include a current limit that is more sensitive in the MT strategy, the following 4 inequality constraints are defined based on (19),

$$
\begin{cases}
g_1: & \sqrt{(K_X^\alpha + 1)^2 + K_X^{\beta 2}} \leq \dfrac{1}{i_{pu}} \\[2mm]
g_2: & \sqrt{(K_X^\alpha + 1)^2 + (K_X^\beta + 2\sqrt{3})^2} \leq \dfrac{2}{i_{pu}} \\[2mm]
g_3: & \sqrt{(K_X^\alpha + 1)^2 + (K_X^\beta - 2\sqrt{3})^2} \leq \dfrac{2}{i_{pu}} \\[2mm]
g_4: & \sqrt{(K_X^\alpha - 1)^2 + K_X^{\beta 2}} \leq \dfrac{2}{\sqrt{3}i_{pu}}
\end{cases}
\tag{30}
$$

To solve this optimisation problem with inequality constraints, graphical means is used to assist the analysis and solution. As shown in Fig. 3(a), these 4 inequality constraints are essentially 4 circles in the $K_X^\alpha K_X^\beta$ plane. Only the combination of K_X^α and K_X^β within the intersection of these 4 circles are feasible to be applied to the post-fault operation under specific condition. It is demonstrated in Fig. 3(a) that the global minimum of (13) lays within the feasible region, meaning that the inequality constrains in (30) are inactive during the ML strategy. As the torque reference continues to increase, i.e. i_{pu} increases accordingly, and the 4 circles shrink towards their own centres, resulting in a shrinking feasible region. It is obvious that the global minimum at the origin is feasible until $i_{pu} = 55.47\%$, above which the ML strategy is no longer feasible, as depicted in Fig. 3(a). Also as demonstrated in *Fig. 3*(d), the only feasible combination of K_X^α and K_X^β with $i_{pu} = 57,735\%$ is (-1,0), which is the intersection point of guidelines of g_2, g_3 and g_4 where they are tangential to one another. This finding is identical to the optimisation result of MT with 2N. Moreover, the feasible region is always symmetrical about the K_X^α axis because of the locations of the centre of those 4 circles. Consequently, in the transient region where some of the inequality constraints are active, the minimum point within the feasible region is always the left vertex, which is the intersection of g_2 and g_3, as shown in Fig. 3(c). This means that within the transient region, regardless of i_{pu}, K_X^β is always 0, and thus K_X^α is calculated as illustrated in (31).

(a) $i_{pu} = 0.5$ (b) $i_{pu} = 0.5547$ (c) $i_{pu} = 0.566$ (d) $i_{pu} = 0.5774$
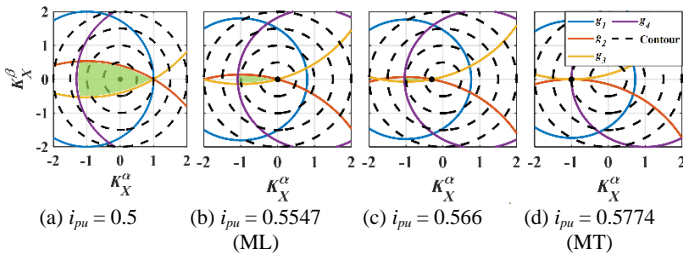(ML) (MT)

Fig. 3 Contour of objective function in (18) and guidelines of the 4 inequality constraints in (30)

Therefore, the analytical solution of the optimum parameters of 2N in 1OCF can be summarised in (32) and implemented in the control scheme as shown in Fig. 4.

$$
K_X^\alpha = -1 + \sqrt{\frac{4}{i_{pu}^2} - 12}.
\tag{31}
$$

$$
\begin{cases}
K_X^\alpha = 0 \quad \left(i_{pu} \leq \dfrac{2}{\sqrt{13}}\right) \\[2mm]
K_X^\alpha = -1 + \sqrt{\dfrac{4}{i_{pu}^2} - 12} \quad \left(\dfrac{2}{\sqrt{13}} < i_{pu} \leq \dfrac{\sqrt{3}}{3}\right) \\[2mm]
K_X^\beta = K_Y^\alpha = 0 \\[2mm]
K_Y^\beta = -1
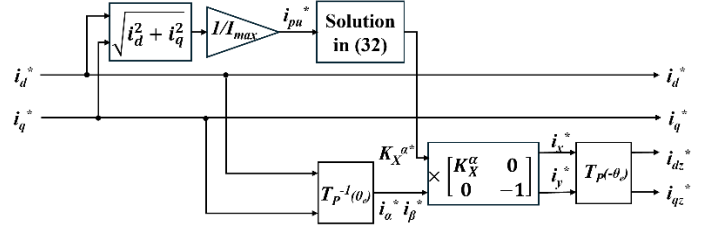\end{cases}
\tag{32}
$$

Fig. 4 Implementation of FTOR-ML for 2N

2. Single Neutral Point (1N)

In the case of single neutral point, the graphical means is no longer feasible as there are 4 design variables. Hence, the Karush-Kuhn-Tucker (KKT) approach is applied to solve the optimisation problem with inequality constraints, using Lagrange multipliers, defined as,

$$
\mathcal{L}(K, \mu_n, s_n) = F(K) + \sum_n \mu_n[g_n(K) + s_n^2]
\tag{33}
$$

where μ_n ($n = 1,2,3,4,5$) is the Lagrange multiplier; $K = [K_X^\alpha\ K_X^\beta\ K_Y^\alpha\ K_Y^\beta]$; $F(K) = K_X^{\alpha 2} + K_X^{\beta 2} + 3K_Y^{\alpha 2} + 3K_Y^{\beta 2} + 4K_Y^\beta + 2$; s_n is the slack variable. Similarly, recalling from M_{1N} in (29), the inequality constraints g_n is defined by the current limit in (35). According to the KKT theorem, to find the extremum of (33), each term of the Jacobian Matrix is equal to zero, which is presented in (A1)-(A6) in Appendix. The derived equation set is extremely difficult to solve because of the complementary slackness in (33), where either $\mu_n = 0$ or $s_n = 0$ and $\mu_n > 0$.

If $\mu_n = 0$, the corresponding inequality constraint is inactive, meaning that $g_n < 0$; if $s_n = 0$ and $\mu_n > 0$, the corresponding inequality constraint is active with $g_n = 0$. The complementary slackness essentially results in $2^5 = 32$ scenarios, and hence the same number of equations in the set to be solved, which is not efficient mathematically.

In this specific case where variables and the inequality constraints have physical meaning, random complementary slackness can be avoided. The inequality constraints are define because of the current limit in each phase winding which cannot be exceeded, to avoid excessive hot spots. The derived optimum design variable K_n^m of 1N using ML strategy in (23) is essentially the solution of this optimisation problem when all the inequality constraints in (35) are inactive. Recalling from the corresponding phase current waveform in (28), it is apparent that current in phase c would reach the current limit first because of its highest phase current coefficient of 1.84 while the rest stay below the limit. Therefore, the third inequality constraint, that corresponds to phase c becomes active while the rest remain inactive until one of the other phase currents reaches the current limit. Mathematically, this is when the coefficient of such phase current equals that of phase c. From this point on, there are 2 phase currents, including phase c, that have reached the current limit, and their corresponding inequality constraints are active until the next phase current also reaches the limit. This process repeats until all 5 phase

currents reach the current limit, with the same current waveform coefficient mathematically. This is essentially the MT strategy where current usage is maximised in the most efficient way to deliver maximum torque, as demonstrated in (27). Therefore, the FTOR-ML with 1N has 5 stages, where the first stage starts from $i_{pu} = 0$ to $i_{pu} = 0.5418$ without any active inequality constraints and the second to fifth stage until $i_{pu} = 0.6944$ with corresponding active inequality constraints. Stage 1 is the ML strategy with its corresponding optimum K_n^m in (23). The K_n^m for the second stage, on the other hand, must be derived by solving the equation set defined by the KKT condition of the optimisation problem. Based on the analysis above that only the third inequality constraint is active, we have $\mu_1, \mu_2, \mu_4, \mu_5$ and $s_3 = 0$. Hence, the KKT condition yields the equation set for stage 2 with 5 unknowns, K_n^m and μ_3, which is presented in A7. It is worth noting that equations involving s_1, s_2, s_4 and s_5 are ignored in the equation set because the design variable K_n^m is independent and their solution are not of interest. The analytical solution is given in (36). For the sake of simplicity, further derivation of K_X^α K_X^β and K_Y^β won't be given.

The first half of Fig. 7 for stage 2 depicts the coefficient of the phase current waveform on the second stage of FTOR-ML with 1N based on the solution given in (36) against the i_{pu}. It can be observed that while the current coefficient of the saturated phase c decreases, the rest of the phase current coefficient increase, resulting in a higher torque output as expected. Phase b intersects with phase c first when $i_{pu} = 0.6485$ while the rest remain unsaturated. This means that from this point on, the stage 3 of FTOR-ML begins and the second and third inequality constraints corresponding to phase b and c are active, meaning μ_1, μ_4, μ_5 and $s_2, s_3 = 0$. Hence, the KKT condition of the third stage, ignoring the slack variable s_1, s_4 and s_5, is defined and shown in (A8). However, this equation set has no analytical solution because it can only be simplified and manipulated to a single equation of one variable of degree of 6. This can be proved by the fact that there are 6 sets of numerical solution with an arbitrarily chosen i_{pu} calculated in Mathematica. According to the Abel-Ruffini Theorem, there is no solution in radicals of equation of degree of 5 or higher. Therefore, Mathematica is used to calculate the numerical solution of such an equation set with respect to i_{pu} starting from $i_{pu} = 0.6485$.

A simple "while" loop is used, as shown in Fig. 5, to find the relation between the 4 design variables and i_{pu} in the third stage. In order to find the right solution within all of the numerical solutions calculated by Mathematica, the solution of the current iteration is used as the initial guess for the next iteration so that a continuous curve of the 4 design variables is guaranteed. It is obvious that the selection of δi_{pu} directly relates to the continuity of the curves of those design variables. The smaller the δi_{pu} the more continuous the curve. The loop stops when one of the current coefficients of the unsaturated phase is equal or higher than the saturated phase. As such, the newly saturated phase indicates that its corresponding inequality constraint

become active in the next stage. The numerical result suggests that phase u is the newly saturated phase during stage 3. Hence, the equation set to be solved for stage 4 with inequality constraints g_2, g_3 and g_4 active (μ_1, μ_5 and $s_2, s_3, s_4 = 0$) can be constructed in (A9). There is no analytical solution for this equation set with 7 variables neither and thus the same methodology is applied, which is followed by the fifth stage with its equation set (A10) to be solved. It is worth noting that the equation set for the fifth stage only consists of 4 equations, all defined by the 4 inequality constraints, because the Lagrange Multipliers are not of interest.

To summarise the analysis and calculation, the 5 stages of FTOR-ML is obtained regarding to i_{pu} as,

$$\begin{cases} Stage\ 1: i_{pu} \le 0.542 \\ Stage\ 2: 0.542 < i_{pu} \le 0.649 \\ Stage\ 3: 0.649 < i_{pu} \le 0.673 \\ Stage\ 4: 0.673 < i_{pu} \le 0.688 \\ Stage\ 5: 0.688 < i_{pu} \le 0.694 \end{cases} \quad (34)$$

and the 4 design variables derived for each stage are shown in Fig. 6. Their corresponding phase current coefficient are depicted in Fig. 7. Finally, the control scheme is implemented in Fig. 8.
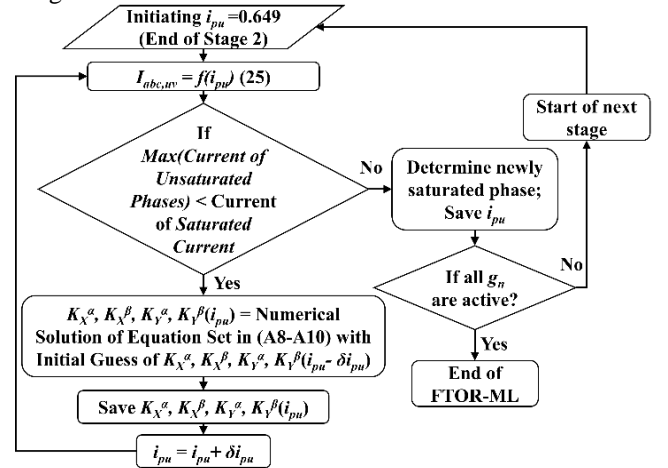

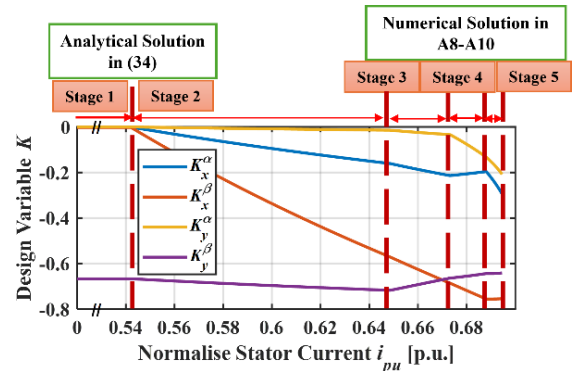*Fig. 5 Flow chart to calculate the design variables of stage 2-5 of FTOR-ML*

Fig. 6 Design variable for FTOR-ML with 1N

$$\begin{cases} g_1: (K_X^\alpha - K_Y^\alpha + 1)^2 + (K_X^\beta - K_Y^\beta - 1)^2 - \dfrac{1}{i_{pu}^2} \le 0 \\[2mm] g_2: \left[K_X^\alpha + (\sqrt{3}+2)K_Y^\alpha + 1\right]^2 + \left[K_X^\beta + (\sqrt{3}+2)K_Y^\beta + 2 - \sqrt{3}\right]^2 - \dfrac{4}{i_{pu}^2} \le 0 \\[2mm] g_3: \left[K_X^\alpha - (\sqrt{3}-2)K_Y^\alpha + 1\right]^2 + \left[K_X^\beta - (\sqrt{3}-2)K_Y^\beta + 2 + \sqrt{3}\right]^2 - \dfrac{4}{i_{pu}^2} \le 0 \\[2mm] g_4: (K_X^\alpha - \sqrt{3}K_Y^\alpha - 1)^2 + (K_X^\beta - \sqrt{3}K_Y^\beta - \sqrt{3})^2 - \dfrac{4}{3i_{pu}^2} \le 0 \\[2mm] g_5: (K_X^\alpha + \sqrt{3}K_Y^\alpha - 1)^2 + (K_X^\beta + \sqrt{3}K_Y^\beta + \sqrt{3})^2 - \dfrac{4}{3i_{pu}^2} \le 0 \end{cases} \quad (35)$$

$$\begin{cases} K_X^\alpha = (6 + 3\sqrt{3})\,K_Y^\alpha \\[2mm] K_X^\beta = (6 + 3\sqrt{3})K_Y^\beta + 4 + 2K_Y^\beta \\[2mm] K_Y^\alpha = \dfrac{\sqrt{\dfrac{198 - 45\sqrt{3}}{409}} - i_{pu}}{(8 + 2\sqrt{3})i_{pu}} \\[3mm] K_Y^\beta = \dfrac{(2 + 5\sqrt{3})K_Y^\alpha - 2}{3} \end{cases} \quad (36)$$
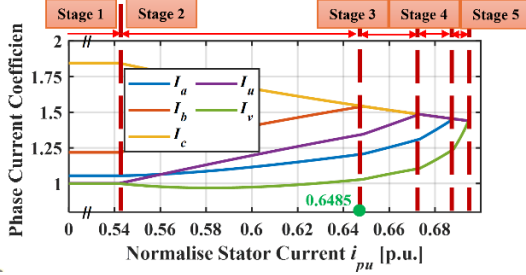
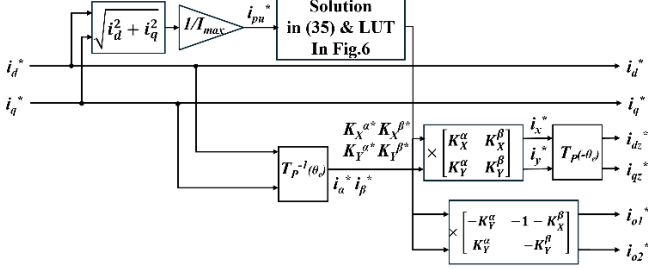*Fig. 7 Phase current coefficient for FTOR-ML with 1N*

Fig. 8 Implementation of FTOR-ML for 1N

Table 2 Motor parameters of DT-PMSM

Parameter	Value	Parameter	Value
No. of Pole Pair	4	L_d [mH]	0.293
Ω_n [rev/min]	3000	L_q [mH]	0.7
U_{dc} [V]	120	L_{dz} [mH]	0.017
I_{max} [A]	24	L_{qz} [mH]	0.017
Te_n [Nm]	12.6	L_{o1} [mH]	0.011
R_s [Ω]	0.042	L_{o2} [mH]	0.011
Ψ_f [Wb]	0.044		

IV. SIMULATION AND EXPERIMENTAL INVESTIGATION ON THE FTOR-ML

To verify the effectiveness of the proposed FTC strategy, simulation is performed, and a test rig is setup to implement the algorithm of FTOR-ML. Table 2 shows the key parameters of the DT-PMSM for simulation and experimental testing. The inductances in each synchronous frame were measured by a sequence of test procedure demonstrated in [20].

A. Numerical Simulation

The post-fault mathematical model of the DT-PMSM derived in section II is built in MATLAB/Simulink.

To verify the proposed control scheme, based on the control scheme demonstrated in Fig. 2, a sequence of reference torques is applied to the model at motor speed of 500 RPM. This sequence is constructed so that each step of the corresponding reference current vector magnitude lays in different stage of the TOR. The corresponding reference current is calculated by the MTPA scheme.

As shown in Fig. 9(a) for 2N, the first and second step correspond to the conventional ML. None of the phase currents have reached the current limit in the first step whereas phase b and c have saturated in the second step. To further increase the torque reference in the third step, the proposed FTOR-ML becomes active and while the current magnitude of phase b and c are maintained, currents in phase u and v start to increase to boost the torque output. In the final step, all phase currents, except phase a, are saturated for maximum torque output under single OCF. The current decreasing in phase a, after the TOR of ML, is the result of the nature of the mathematical solution derived for the FTOR-ML. It is worth noting that the reference torque is not linear against its corresponding current vector magnitude. This is due to the non-linear MTPA scheme of IPM that results in non-linear relation between the torque and current references.

Fig. 9 (b) presents a similar simulation process for single neutral point. The result is as expected, where phase c saturates first, following by phase b, u, a, and finally phase v.
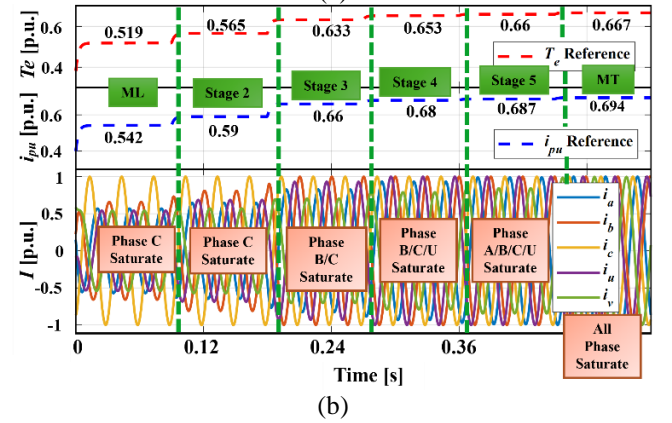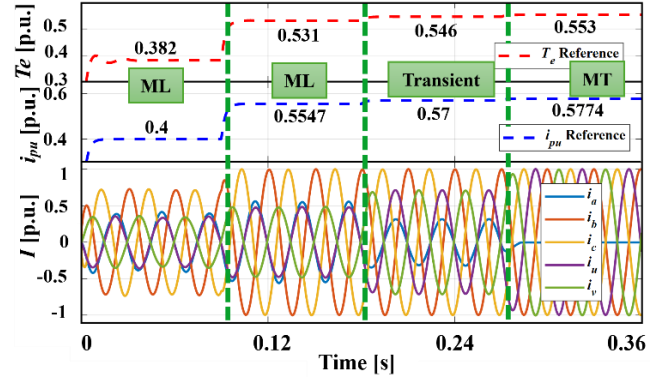

(a)

(b)

Fig. 9 Simulating motor dynamics for (a) 2N and (b) 1N under single OCF by FTOR-ML (Top: reference torque sequence; Middle: current vector magnitude i_{pu}; Bottom: phase current waveform)

B. Experimental Setup

Fig. 10 shows the schematic diagram of the back-to-back test platform developed for the experimental validation, depicting the arrangement of components, sensors and interfaces. On this basis, Fig. 11 shows the actual setup in the test cell, where the motor under testing (DT-PMSM) is placed on a test rig, and a dynamometer (Induction Motor) operates as a prime mover under speed control to regulate the shaft speed. The dynamometer has its own drive and power supply so that the two machines are decoupled electrically. The DT-PMSM is driven by an inverter consisting 6 identical half-bridge modular units (Imperix PEB8024). Current sensors are mounted on each AC output of these units for current measurement. The FOC and proposed FTC scheme are implemented in the controller (Imperix B-Box), from which PWM signals are generated and fed to the inverter through optical fibre. There is also an additional interface to read and interpret the resolver signal for rotor position measurement. It will be seen that there is a connection box placed between the drive cabinet and the DT-PMSM, to connect the power cables, with a circuit breaker mounted inside, to either connect or isolate the 2 neutral points to form the 2 different winding configurations, as shown in the schematic in Fig. 10.

Before implementing the FTC, the motor runs in healthy condition with an anti-windup PI controller in DQ- and DQz-frame and 3rd resonant controller in zero-sequence subspace as outlined in Fig. 2, with no harmonics suppression control (HSC) introduced. However, due to the nature of non-linearity from various sources, e.g. magnetic saturation/non-sinusoidal back EMF/dead time effects in the inverter, harmonics current is

inevitably introduced to form a distorted phase current waveform. Fig. 12 shows the current waveform on 2N and 1N when HSC is not included. The 5th/7th and 11th/13th harmonics components dominate in the waveform, which are the exact result of those aforementioned non-linearities [20-22]. Therefore, HSC is introduced in order to have a cleaner and less-distorted current waveform during the single-phase OCF. As demonstrated in [13, 20, 21], a 6th resonant controller is introduced in DQz-frame to regulate the 5th/7th harmonics, while 11th/13th harmonics are suppressed by a 12th resonant controller in DQ-frame. The effectiveness of the HSC is demonstrated in Fig. 12 that the total harmonic distortion values are improved from 8.61% and 8.81% to 3.1% and 3.38% for 2N and 1N respectively. More specifically, the 5th/7th and 11th/13th harmonics components are significantly suppressed.
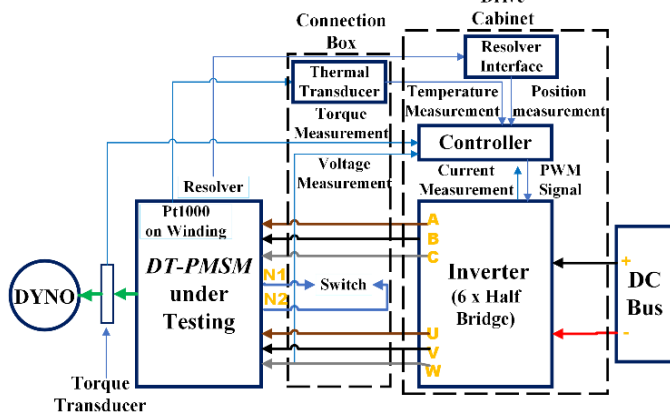

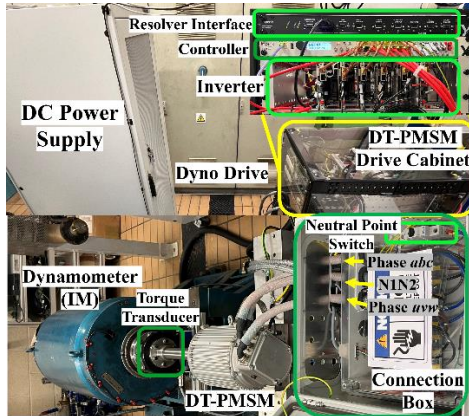
Fig. 10 Schematic of DT-PMSM experimental platform

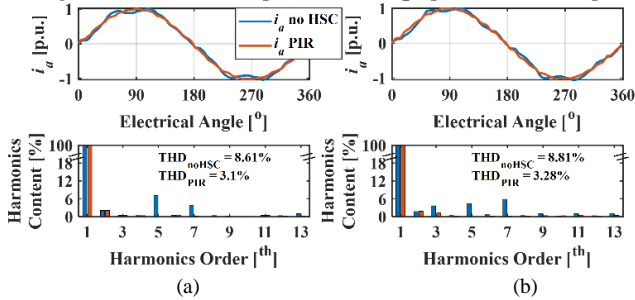*Fig. 11 DT-PMSM experimental equipment and setup*

Fig. 12 Current waveform comparison of phase a with or without harmonics suppression (a) 2N (b) 1N

C. Experimental Result of the Proposed FTOR-ML

Three sets of experiment have been carried out to validate the proposed FTOR-ML. The first and second set mimic the same current reference sequence as the simulation, for 2N and 1N respectively, to demonstrate the effectiveness of the proposed control scheme. The third set studies the copper loss to validate the superiority of the minimum losses throughout the entire TOR.

During the first experiment, the same sequence of current reference as the simulation has been applied to the faulty DT-PMSM with 2N. Since the dynamometer does not have good low-speed stability, the test was carried out at 500 RPM, which is not high enough to induce distorted current. As shown in *Fig. 13*, the reference i_{pu} is followed and no phase current has exceeded the limitation. The current waveforms of the phases in each step of the sequence, as depicted in Fig. 13(b)-(e), were as expected and corresponded to the analysis in III.B.1 and simulation results in IV.B, despite the slightly distorted component. The torque output, which is measured by a torque transducer (HBM T40B) mounted on the shaft, is smooth and almost ripple-free throughout the sequence in Fig. 13(a). However, in the actual torque waveform, 6th-order ripple is noticeable, especially in ② and ③. This means that the superiority of DT-PMSM without 6th-order torque ripple is not preserved during single-phase OCF. The reason is that the 5th and 7th current harmonics corresponding to 6th harmonics in the synchronous frame cannot be fully decoupled due to the loss of one phase, resulting in the presence of 6th harmonic current in the torque-relevant DQ-frame and hence 6th-order torque ripple. It should be noted that the motor parameters used for the mathematical model in the numerical simulation were measured under healthy condition. However, when the motor is in single-phase OCF, it becomes highly unbalanced and hence the inductances and flux linkages under load condition are affected. Consequently, the average torque output in each step of the sequence in the experiment, is slightly different from that in the simulation.
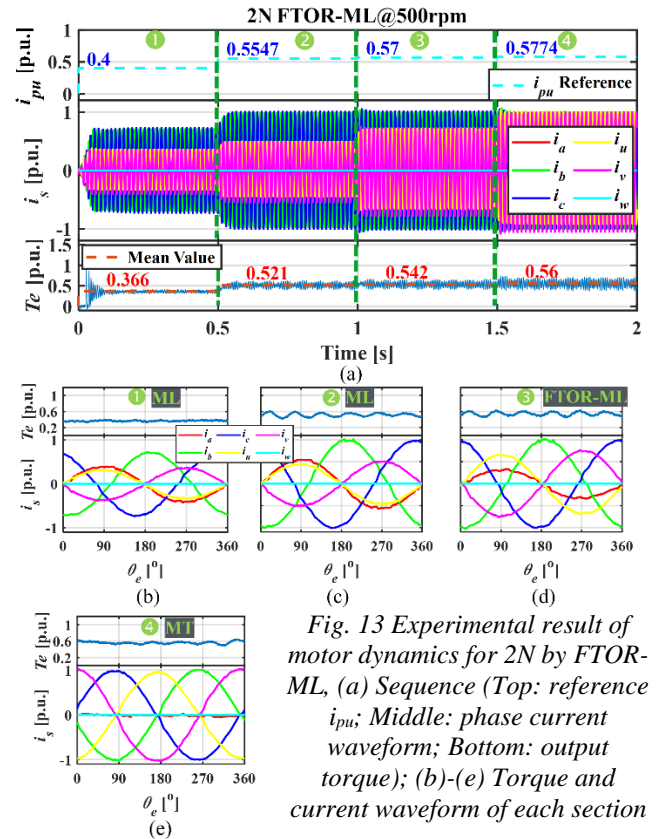

Fig. 13 Experimental result of motor dynamics for 2N by FTOR-ML, (a) Sequence (Top: reference i_{pu}; Middle: phase current waveform; Bottom: output torque); (b)-(e) Torque and current waveform of each section

In the second experiment for 1N, as presented in Fig. 14, the test outcome matches the analytical solution and numerical simulation. Despite the slight high-frequency distortion, the current waveforms were sinusoidal and phase *c/b/u/a* and *v* saturated from step to step that corresponds to each stage of the FTOR-ML of 1N derived in III.B.2. Similar to the case of 2N, apart from the small 6th-order ripple, the electromagnetic torque was maintained at certain level in each step.
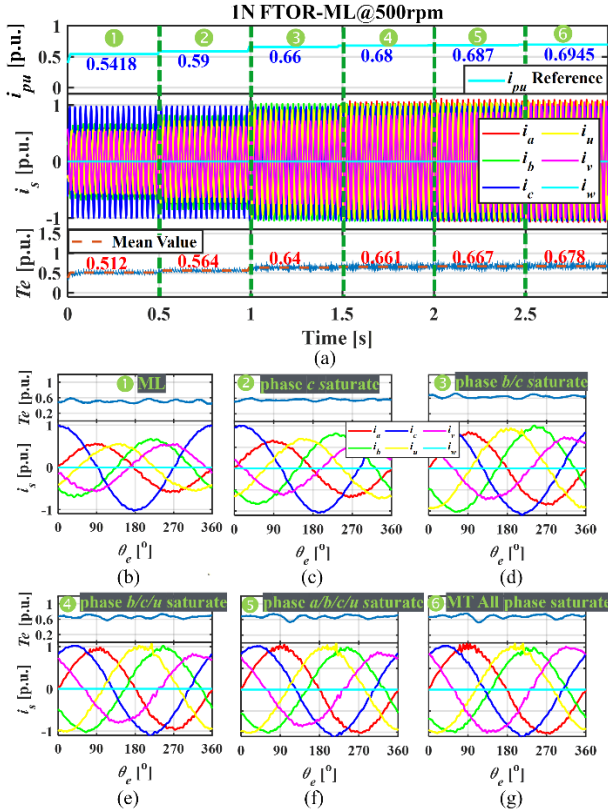
Fig. 14 Experimental result of motor dynamics for 1N by FTOR-ML, (a) Sequence (Top: reference i_{pu}; Middle: phase current waveform; Bottom: output torque); (b)-(g) torque and current waveform of each section

During the third test, the copper loss of the faulty machine for the entire TOR for 2N and 1N was tested and studied. The copper loss is compared to that of the DT-PMSM under healthy condition at maximum load, i.e. $i_{pu} = 1$. It is illustrated in Fig. 15(a) that the proposed FTOR-ML demonstrates minimum copper loss in the transient part between the TOR of ML and MT for 2N. More specifically, Table 3 extracts some of the data from Fig. 15(a) for copper loss and maximum phase current (in p.u.) comparison. While the FTOR-ML corresponds to the same outcome as ML at $i_{pu}^* = 0.5547$ and MT at $i_{pu}^* = 0.5774$, it demonstrates, as anticipated, the trade-off between low copper loss (51.9% for FTOR-ML over 65% for MT) and requirement of not exceeding current limitation to avoid excessive heat point (100% of current usage for FTOR-ML over 102.8% for ML).

Similarly, for 1N, the FTOR-ML demonstrates minimum copper loss throughout the TOR, as shown in Fig. 15(b). Table 4 compares performance among the ML, MT and proposed FTOR-ML. Within the range of i_{pu}^* between 0.5418 and 0.6944, FTOR-ML, again, illustrates good compromise between minimising copper loss and avoiding excessive heat. For instant, at $i_{pu}^* = 0.59$, although the maximum phase current under MT reaches 85% of the limitation (as in FTOR-ML), the total copper loss is 25% higher than that under FTOR-ML (0.602 over 0.48). At $i_{pu}^* = 0.64$, while the copper loss under ML is lower than that under FTOR-ML, the maximum phase current exceeds the limitation by 18.1%, which could result in catastrophic failure due to excessive heat.

It is well-evidenced that, based on the outcome in Fig. 15, Table 3 and Table 4, the propose FTOR-ML has filled the gap of the 2 conventional strategies, ML and MT, to deliver reference torque while maintaining minimum loss. Moreover, the test data has shown great alignment with the analytical result. These 2 tests have further verified the effectiveness of the proposed control scheme.
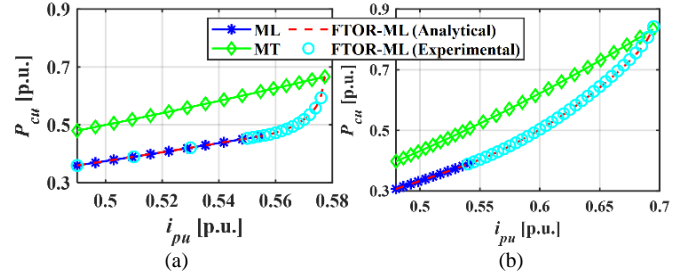

Fig. 15 Copper loss comparison for (a) 2N and (b) 1N between ML/MT and FTOR-ML

Table 3 Comparison between different control schemes for 2N

i_{pu}^*	0.5547		0.57		0.5774	
	P_{cu}	I_{max}	P_{cu}	I_{max}	P_{cu}	I_{max}
ML	0.462	1	0.493	1.028	0.505	1.041
MT	0.615	0.961	0.65	0.987	0.667	1
FTOR-ML	0.462	1	0.519	1	0.667	1

Table 4 Comparison between different control schemes for 1N

i_{pu}^*	0.5418		0.59		0.64		0.6944	
	P_{cu}	I_{max}	P_{cu}	I_{max}	P_{cu}	I_{max}	P_{cu}	I_{max}
ML	0.391	1	0.464	1.09	0.5456	1.181	0.642	1.281
MT	0.507	0.781	0.602	0.85	0.708	0.922	0.833	1
FTOR-ML	0.391	1	0.48	1	0.61	1	0.833	1

V. CONCLUSION

This paper has derived the mathematical model for a post-fault asymmetrical dual three-phase PMSM under single open-circuit fault (OCF). Based on the model, a fault-tolerant control scheme that is applicable for the entire torque operation range with minimum copper loss has been proposed. Winding topologies with both single and isolated neutral point have been considered. The proposed FTOR-ML scheme has successfully combined the merits of minimum loss and maximum torque. The torque operation range (TOR) of ML has been extended to that of MT, where minimum copper loss is achieved throughout the entire TOR (0-57.74% and 0-69.94% of rated torque for 2N and 1N respectively), which is validated by numerical simulation and a series of experiments. The analytical solution for the design variables is derived which significantly reduces the complexity of the control scheme and also the computation effort required without the use of conventional look-up tables.

VI. REFERENCE

[1] G. H. Liu, J. Q. Yang, W. X. Zhao, J. H. Ji, Q. Chen, and W. S. Gong, "Design and Analysis of a New Fault-Tolerant Permanent-Magnet Vernier Machine for Electric Vehicles," *IEEE Transactions on Magnetics,* vol. 48, no. 11, pp. 4176-4179, Nov 2012.

[2] R. Bojoi, S. Rubino, A. Tenconi, and S. Vaschetto, "Multiphase Electrical Machines and Drives: A Viable Solution for Energy Generation and Transportation Electrification," *Int Conf Expo Electr,* pp. 632-639, 2016.

[3] N. Bianchi *et al.*, "Permanent magnet synchronous motor drives for more-electric aircraft," presented at the 2022 International Symposium on Power Electronics, Electrical Drives, Automation and Motion (SPEEDAM), Sorrento, Italy, 2022.

[4] P. Wheeler, T. S. Sirimanna, S. Bozhko, and K. S. Haran, "Electric/Hybrid-Electric Aircraft Propulsion Systems," *P Ieee,* vol. 109, no. 6, pp. 1115-1127, Jun 2021.

[5] M. J. B. Duran, F., "Recent Advances in the Design, Modeling, and Control of Multiphase Machines-Part II," *IEEE Transactions on Industrial Electronics,* vol. 63, no. 1, pp. 459-468, Jan 2016.

[6] H. S. Che, M. J. Duran, E. Levi, M. Jones, W. P. Hew, and N. Abd Rahim, "Postfault Operation of an Asymmetrical Six-Phase Induction Machine With Single and Two Isolated Neutral Points," *IEEE Transactions on Power Electronics,* vol. 29, no. 10, pp. 5406-5416, Oct 2014.

[7] K. L. Yu, Z. Wang, M. R. Gu, and X. Q. Wang, "Universal Control Scheme of Dual Three-Phase PMSM Drives With Single Open-Phase Fault," *IEEE Transactions on Power Electronics,* vol. 37, no. 12, pp. 14034-14039, Dec 2022.

[8] J. Cui, J. H. Ji, W. X. Zhao, T. Tao, L. S. Huang, and H. Y. Tang, "Decoupled Fault-Tolerant Model Predictive Current Control for Dual Three-Phase PMSMs With Harmonic Compensation," *IEEE Transactions on Power Electronics,* vol. 38, no. 2, pp. 2285-2294, Feb 2023.

[9] J. R. Fu and T. A. Lipo, "Disturbance-Free Operation of a Multiphase Current-Regulated Motor Drive with an Opened Phase," *IEEE Transactions on Industry Applications,* vol. 30, no. 5, pp. 1267-1274, Sep-Oct 1994.

[10] S. Dwari and L. Parsa, "Fault-Tolerant Control of Five-Phase Permanent-Magnet Motors With Trapezoidal Back EMF," *IEEE Transactions on Industrial Electronics,* vol. 58, no. 2, pp. 476-485, Feb 2011.

[11] R. S. Arashloo, J. L. R. Martinez, M. Salehifar, and M. Moreno-Eguilaz, "Genetic algorithm-based output power optimisation of fault tolerant five-phase brushless direct current drives applicable for electrical and hybrid electrical vehicles," *Iet Electr Power App,* vol. 8, no. 7, pp. 267-277, Aug 2014.

[12] W. Wang, J. H. Zhang, M. Cheng, and S. H. Li, "Fault-Tolerant Control of Dual Three-Phase Permanent-Magnet Synchronous Machine Drives Under Open-Phase Faults," *IEEE Transactions on Power Electronics,* vol. 32, no. 3, pp. 2052-2063, Mar 2017.

[13] H. M. Eldeeb, A. S. Abdel-Khalik, and C. M. Hackl, "Postfault Full Torque Speed Exploitation of Dual Three-Phase IPMSM Drives," *IEEE Transactions on Industrial Electronics,* vol. 66, no. 9, pp. 6746-6756, Sep 2019.

[14] Y. S. Hu, Y. J. Feng, and X. F. Li, "Fault-Tolerant Hybrid Current Control of Dual Three-Phase PMSM With One Phase Open," *IEEE Journal of Emerging and Selected Topics in Power Electronics,* vol. 10, no. 3, pp. 3418-3426, Jun 2022.

[15] Q. Geng, Z. C. Li, H. M. Wang, G. Z. Zhang, and Z. Q. Zhou, "Natural Fault-Tolerant Control With Minimum Copper Loss in Full Torque Operation Range for Dual Three-Phase PMSM Under Open-Circuit Fault," *IEEE Transactions on Power Electronics,* vol. 39, no. 1, pp. 1279-1291, Jan 2024.

[16] J. Zou, C. Liu, Y. Xu, and G. Yu, "Open-Circuit Fault-Tolerant Control for Dual Three-Phase PMSM With Minimum Torque Ripple Considering Phase Back EMF Harmonics," *IEEE Transactions on Transportation Electrification,* vol. 10, no. 1, pp. 1508 - 1518, March 2024.

[17] J. W. Sun, Z. C. Liu, Z. D. Zheng, and Y. D. Li, "An Online Global Fault-Tolerant Control Strategy for Symmetrical Multiphase Machines With Minimum Losses in Full Torque Production Range," *IEEE Transactions on Power Electronics,* vol. 35, no. 3, pp. 2819-2830, Mar 2020.

[18] H. Zheng, X. Pei, and C. Brace, "Full Torque Operation Range Fault-Tolerant Control with Minimum Copper Loss for Dual Three-Phase PMSM," presented at the 2023 11th International Conference on Power Electronics and ECCE Asia (ICPE 2023 - ECCE Asia), Jeju Island, Korea, Republic of, 2023.

[19] Y. Zhao and T. A. Lipo, "Space vector PWM control of dual three-phase induction machine using vector space decomposition," *IEEE Transactions on Industry Applications* vol. 31, no. 5, Sept.-Oct. 1995, pp. 1100 - 1109, 1995.

[20] H. M. Eldeeb, A. S. Abdel-Khalik, and C. M. Hackl, "Dynamic Modeling of Dual Three-Phase IPMSM Drives With Different Neutral Configurations," *IEEE Transactions on Industrial Electronics,* vol. 66, no. 1, pp. 141-151, Jan 2019.

[21] Y. S. Hu, Z. Q. Zhu, and K. Liu, "Current Control for Dual Three-Phase Permanent Magnet Synchronous Motors Accounting for Current Unbalance and Harmonics," *IEEE Journal of Emerging and Selected Topics in Power Electronics,* vol. 2, no. 2, pp. 272-284, Jun 2014.

[22] A. G. Yepes, J. Doval-Gandoy, F. Baneira, D. Pérez-Estévez, and O. López, "Current Harmonic Compensation for n-Phase Machines With Asymmetrical Winding Arrangement and Different Neutral Configurations," *IEEE Transactions on Industry Applications,* vol. 53, no. 6, pp. 5426-5439, Nov-Dec 2017.

Appendix

Each term of the Jacobian Matrix of the Lagrange Equation in (33) is expressed as,

$$\frac{\partial \mathcal{L}}{\partial K_X^\alpha} = 2K_X^\alpha + 2\mu_1(K_X^\alpha - K_Y^\alpha + 1) + 2\mu_2[K_X^\alpha + (\sqrt{3}+2)K_Y^\alpha + 1] + 2\mu_3[K_X^\alpha - (\sqrt{3}-2)K_Y^\alpha + 1] +$$
$$2\mu_4(K_X^\alpha - \sqrt{3}K_Y^\alpha - 1) + 2\mu_5(K_X^\alpha + \sqrt{3}K_Y^\alpha - 1) = 0 \tag{A1}$$

$$\frac{\partial \mathcal{L}}{\partial K_X^\beta} = 2K_X^\beta + 2\mu_1(K_X^\beta + K_Y^\beta + 1) + 2\mu_2[K_X^\beta + (\sqrt{3}+2)K_Y^\beta + 2 - \sqrt{3}] +$$
$$2\mu_3[K_X^\beta - (\sqrt{3}-2)K_Y^\beta + 2 + \sqrt{3}] + 2\mu_4(K_X^\beta - \sqrt{3}K_Y^\beta - \sqrt{3}) + 2\mu_5(K_X^\beta + \sqrt{3}K_Y^\beta + \sqrt{3}) = 0 \tag{A2}$$

$$\frac{\partial \mathcal{L}}{\partial K_Y^\alpha} = 6K_Y^\alpha - 2\mu_1(K_X^\alpha - K_Y^\alpha + 1) + 2(\sqrt{3}+2)\mu_2[K_X^\alpha + (\sqrt{3}+2)K_Y^\alpha + 1] -$$
$$2(\sqrt{3}-2)\mu_3[K_X^\alpha - (\sqrt{3}-2)K_Y^\alpha + 1] - 2\sqrt{3}\mu_4(K_X^\alpha - \sqrt{3}K_Y^\alpha - 1) + 2\sqrt{3}\mu_5(K_X^\alpha + \sqrt{3}K_Y^\alpha - 1) = 0 \tag{A3}$$

$$\frac{\partial \mathcal{L}}{\partial K_Y^\beta} = 6K_Y^\beta + 4 + 2\mu_1(K_X^\beta + K_Y^\beta + 1) + 2(\sqrt{3}+2)\mu_2[K_X^\beta + (\sqrt{3}+2)K_Y^\beta + 2 - \sqrt{3}] -$$
$$2(\sqrt{3}-2)\mu_3[K_X^\beta - (\sqrt{3}-2)K_Y^\beta + 2 + \sqrt{3}] - 2\sqrt{3}\mu_4(K_X^\beta - \sqrt{3}K_Y^\beta - \sqrt{3}) + 2\sqrt{3}\mu_5(K_X^\beta + \sqrt{3}K_Y^\beta + \sqrt{3}) = 0 \tag{A4}$$

$$\frac{\partial \mathcal{L}}{\partial \mu_n} = g_n + s_n^2 = 0, (n = 1,2,3,4,5) \tag{A5}$$

$$\frac{\partial \mathcal{L}}{\partial s_n} = 2\mu_n s_n = 0, (n = 1,2,3,4,5) \tag{A6}$$

The equation set for stage 2, 3, 4 and 5 of the FTOR-ML with 1N are defined by their corresponding active inequality constraints, where only A7 has analytical solution. Equation sets are expressed as

$$\begin{cases} K_X^\alpha + \mu_3[K_X^\alpha - (\sqrt{3}-2)K_Y^\alpha + 1] = 0 & ① \\ K_X^\beta + \mu_3[K_X^\beta - (\sqrt{3}-2)K_Y^\beta + 2 + \sqrt{3}] = 0 & ② \\ 3K_Y^\alpha - (\sqrt{3}-2)\mu_3[K_X^\alpha - (\sqrt{3}-2)K_Y^\alpha + 1] = 0 & ③ \\ 3K_Y^\beta + 2 - (\sqrt{3}-2)\mu_3[K_X^\beta - (\sqrt{3}-2)K_Y^\beta + 2 + \sqrt{3}] = 0 & ④ \\ [K_X^\alpha - (\sqrt{3}-2)K_Y^\alpha + 1]^2 + [K_X^\beta - (\sqrt{3}-2)K_Y^\beta + 2 + \sqrt{3}]^2 = \frac{4}{i_{pu}^2} & ⑤ \end{cases} \tag{A7}$$

$$\begin{cases} K_X^\alpha + \mu_2[K_X^\alpha + (\sqrt{3}+2)K_Y^\alpha + 1] + \mu_3[K_X^\alpha - (\sqrt{3}-2)K_Y^\alpha + 1] = 0 & ① \\ K_X^\beta + \mu_2[K_X^\beta + (\sqrt{3}+2)K_Y^\beta + 2 - \sqrt{3}] + \mu_3[K_X^\beta - (\sqrt{3}-2)K_Y^\beta + 2 + \sqrt{3}] = 0 & ② \\ 3K_Y^\alpha + (\sqrt{3}+2)\mu_2[K_X^\alpha + (\sqrt{3}+2)K_Y^\alpha + 1] - (\sqrt{3}-2)\mu_3[K_X^\alpha - (\sqrt{3}-2)K_Y^\alpha + 1] = 0 & ③ \\ 3K_Y^\beta + 2 + (\sqrt{3}+2)\mu_2[K_X^\beta + (\sqrt{3}+2)K_Y^\beta + 2 - \sqrt{3}] - (\sqrt{3}-2)\mu_3[K_X^\beta - (\sqrt{3}-2)K_Y^\beta + 2 + \sqrt{3}] = 0 & ④ \\ [K_X^\alpha + (\sqrt{3}+2)K_Y^\alpha + 1]^2 + [K_X^\beta + (\sqrt{3}+2)K_Y^\beta + 2 - \sqrt{3}]^2 = \frac{4}{i_{pu}^2} & ⑤ \\ [K_X^\alpha - (\sqrt{3}-2)K_Y^\alpha + 1]^2 + [K_X^\beta - (\sqrt{3}-2)K_Y^\beta + 2 + \sqrt{3}]^2 = \frac{4}{i_{pu}^2} & ⑥ \end{cases} \tag{A8}$$

$$\begin{cases} K_X^\alpha + \mu_2[K_X^\alpha + (\sqrt{3}+2)K_Y^\alpha + 1] + \mu_3[K_X^\alpha - (\sqrt{3}-2)K_Y^\alpha + 1] + \mu_4(K_X^\alpha - \sqrt{3}K_Y^\alpha - 1) = 0 & ① \\ K_X^\beta + \mu_2[K_X^\beta + (\sqrt{3}+2)K_Y^\beta + 2 - \sqrt{3}] + \mu_3[K_X^\beta - (\sqrt{3}-2)K_Y^\beta + 2 + \sqrt{3}] + \mu_4(K_X^\beta - \sqrt{3}K_Y^\beta - \sqrt{3}) = 0 & ② \\ \begin{aligned} &3K_Y^\alpha + (\sqrt{3}+2)\mu_2[K_X^\alpha + (\sqrt{3}+2)K_Y^\alpha + 1] \\ &-(\sqrt{3}-2)\mu_3[K_X^\alpha - (\sqrt{3}-2)K_Y^\alpha + 1] - \sqrt{3}\mu_4(K_X^\alpha - \sqrt{3}K_Y^\alpha - 1) = 0 \end{aligned} & ③ \\ \begin{aligned} &3K_Y^\beta + 2 + (\sqrt{3}+2)\mu_2[K_X^\beta + (\sqrt{3}+2)K_Y^\beta + 2 - \sqrt{3}] \\ &-(\sqrt{3}-2)\mu_3[K_X^\beta - (\sqrt{3}-2)K_Y^\beta + 2 + \sqrt{3}] - \sqrt{3}\mu_4(K_X^\beta - \sqrt{3}K_Y^\beta - \sqrt{3}) = 0 \end{aligned} & ④ \\ [K_X^\alpha + (\sqrt{3}+2)K_Y^\alpha + 1]^2 + [K_X^\beta + (\sqrt{3}+2)K_Y^\beta + 2 - \sqrt{3}]^2 = \frac{4}{i_{pu}^2} & ⑤ \\ [K_X^\alpha - (\sqrt{3}-2)K_Y^\alpha + 1]^2 + [K_X^\beta - (\sqrt{3}-2)K_Y^\beta + 2 + \sqrt{3}]^2 = \frac{4}{i_{pu}^2} & ⑥ \\ (K_X^\alpha - \sqrt{3}K_Y^\alpha - 1)^2 + (K_X^\beta - \sqrt{3}K_Y^\beta - \sqrt{3})^2 = \frac{4}{3i_{pu}^2} & ⑦ \end{cases} \tag{A9}$$

$$\begin{cases} (K_X^\alpha - K_Y^\alpha + 1)^2 + (K_X^\beta - K_Y^\beta - 1)^2 = \frac{1}{i_{pu}^2} & ① \\ [K_X^\alpha + (\sqrt{3}+2)K_Y^\alpha + 1]^2 + [K_X^\beta + (\sqrt{3}+2)K_Y^\beta + 2 - \sqrt{3}]^2 = \frac{4}{i_{pu}^2} & ② \\ [K_X^\alpha - (\sqrt{3}-2)K_Y^\alpha + 1]^2 + [K_X^\beta - (\sqrt{3}-2)K_Y^\beta + 2 + \sqrt{3}]^2 = \frac{4}{i_{pu}^2} & ③ \\ (K_X^\alpha - \sqrt{3}K_Y^\alpha - 1)^2 + (K_X^\beta - \sqrt{3}K_Y^\beta - \sqrt{3})^2 = \frac{4}{3i_{pu}^2} & ④ \end{cases} \tag{A10}$$